Composites Part B 168 (2019) 66–76

Contents lists available at ScienceDirect

Composites Part B

journal homepage: www.elsevier.com/locate/compositesb

Self-assembled nanostructures of 3D hierarchical faceted-iron oxide containing vertical carbon nanotubes on reduced graphene oxide hybrids for enhanced electromagnetic interface shielding

Rajesh Kumar[a,*], Andrei V. Alaferdov[b], Rajesh K. Singh[c], Ashwani K. Singh[d], Jyoti Shah[e], Ravinder K. Kotnala[e], Kedar Singh[d], Yoshiyuki Suda[a], Stanislav A. Moshkalev[b,**]

[a] Department of Electrical and Electronic Information Engineering, Toyohashi University of Technology, 1-1 Hibarigaokua, Tempaku-cho, Toyohashi, Aichi, 441-8580, Japan
[b] Centre for Semiconductor Components and Nanotechnology (CCS Nano), University of Campinas (UNICAMP), Campinas, 13083-870, Sao Paulo, Brazil
[c] School of Physical & Material Sciences, Central University of Himachal Pradesh (CUHP), Kangra, Dharamshala, HP, 176215, India
[d] School of Physical Sciences, Jawaharlal Nehru University, New Delhi, 110067, India
[e] CSIR- National Physical Laboratory, Dr. K.S. Krishnan Road, New Delhi, 110012, India

ARTICLE INFO

Keywords:
Reduced graphene oxide
Faceted-Fe_3O_4 nanoparticles
Vertical CNTs
Microwave
EMI shielding

ABSTRACT

The self-assembled three dimensional (3D) hybrids nanostructure containing uniform growth of vertical carbon nanotubes (VCNTs) with faceted iron oxide nanoparticles (f-Fe_3O_4 NPs) on the surfaces of reduced graphene oxide nanosheets (rGO NSs) is achieved using microwave assisted approach. The formation of hierarchical 3D f-Fe_3O_4-VCNTs@rGO hybrids, using microwave method is a rapid, simple, and inexpensive synthetic route. First, the VCNTs grow with help of Fe NPs, and after oxidizing of Fe NPs in form of f-Fe_3O_4 NPs, the growth has terminated resulting in formation of small size (< 500 nm) VCNTs containing f-Fe_3O_4 NPs on its tip. The defect- and oxygen-rich sites of rGO NSs favor the heterogeneous nucleation and growth of f-Fe_3O_4 NPs on the tip of VCNTs. The synthesized 3D f-Fe_3O_4-VCNTs@rGO hybrid shows the improved electromagnetic interference (EMI) for microwave shielding effectiveness (SE) as compared to both rGO NSs and Fe_3O_4 NPs@rGO NSs materials. This 3D f-Fe_3O_4-VCNTs@rGO hybrid demonstrates the shielding effectiveness value more than ~25 dB as compared to Fe_3O_4 NPs@rGO NSs for 1.0 mm thin film of 3D f-Fe_3O_4-VCNTs@rGO hybrids in microwave X-band (8.2–12.4 GHz). This applied microwave synthesis approach for 3D f-Fe_3O_4-VCNTs@rGO hybrids is simple, fast, reproducible and scalable for advanced EMI shielding materials. It can be concluded that the faceted Fe_3O_4 NPs on the tip of VCNTs which are grown in-situ on rGO NSs shows synergetic performance for EMI shielding elements in advanced application areas like spacecraft and aircraft.

1. Introduction

Microwave (frequency 0.3–300 GHz; wavelength: 1m-1 mm) absorption materials have attracted plentiful attention for their vital applications in the fields of military aircrafts, environment protection, and communication equipment and the centimeter band wavelengths (2–18 GHz) are extremely important for most of the shielding research focuses on this field [1,2]. With the rapid development of microwave communication equipment and sensitive electronic devices such as mobile phones, local area network systems, radars, wireless data communication, aerospace, television, satellite etc. and its radiation on human life and interactions with sensitive electronic devices has become an increasingly serious problem [3,4]. As a result, protecting sensitive things in terms of information security from electromagnetic (EM) radiation and its leaking have become a serious concern [5,6]. So, nowadays for the absorption of microwave, electromagnetic interference shielding effectiveness (EMI-SE) materials have received considerable attention in advanced communication technologies to protect them from harmful radiation [7,8]. Also, it provides a safe space to electronic devices due to their ability in absorbing electromagnetic waves especially microwave by magnetic and dielectric loss mechanisms [9–11]. The EMI-SE can be achieved by minimizing the signal

* Corresponding author. Department of Electrical and Electronic Information Engineering, Toyohashi University of Technology, 1-1 Hibarigaokua, Tempaku-cho, Toyohashi, Aichi, 441-8580, Japan.
** Corresponding author.
E-mail addresses: rajeshbhu1@gmail.com (R. Kumar), stanisla@ccs.unicamp.br (S.A. Moshkalev).

https://doi.org/10.1016/j.compositesb.2018.12.047
Received 13 May 2018; Received in revised form 4 December 2018; Accepted 13 December 2018
Available online 14 December 2018
1359-8368/

passing through a system either by reflection of the wave or by absorption and dissipation of the radiation power inside and on the surface of the material [12]. Hence, great efforts have been made to develop and achieve promising and meaningful design and synthesis of EMI shielding materials providing high dielectric loss and high magnetic loss with (i) light weight properties, (ii) strong absorption characteristics/minimal reflection characteristics, (iii) wide range of absorption frequency, (iv) thin absorber matching thickness and (v) wide range of absorption frequency [13–15].

Carbon based nanomaterials as well as their heterostructures, specially graphene, a two-dimensional (2D) honeycomb lattice structure composed by sp^2 -bonded carbon atoms, have received extensive attention in EMI shielding due to their unique electrical, mechanical and thermal properties [16–20]. Graphene has a high dielectric loss and exhibits attenuation properties to EM due to its high conductivity [21,22]. However, the large-scale and cheap production of graphene is still a big challenge. In contrast, graphene oxide (GO) and reduced graphene oxide (rGO) as important derivatives of graphene can be produced in large scale owing to the production scalability, low cost and convenient process [23–25]. The rGO also provides a high surface area, thin conducting layered structure and acts as light weight fillers for EMI shielding [13]. However, as rGO has high dielectric loss but low magnetic loss, it cannot meet the actual requirements of impedance match, resulting in the weak EM microwave absorption performance [26–28].

The magnetite materials as Fe_3O_4 containing high magnetic loss has drawn more attention for EMI shielding due to their good magnetic properties, low cost, high abundance, low toxicity, high compatibility and strong spin polarization [13,29,30]. Due to these advantages, Fe_3O_4 is widely studied for EMI shielding. However, pure Fe_3O_4 has been limited hardly in some application areas owing to its poor thermal stability and easy agglomeration which will reduce the EMI shielding [13,31,32]. In order to overcome this problem, decorating magnetic Fe_3O_4 particles onto rGO NSs makes it possible to achieve the desirable EMI shielding material being thin, light-weighted and broadband absorbing. In this case, Fe_3O_4 particles and rGO sheets are acting as magnetic loss and dielectric loss materials, respectively [33].

Recently researchers have shown that rGO with magnetic materials could obtain excellent EM microwave absorption performance for EMI shielding application and demonstrated new kind of synthesized 3D material containing Fe_3O_4-1D carbon nanotube/fiber or Fe_3O_4-2D graphene showing improved application for EMI shielding [21,34–39]. The other emerging 3D material containing the combination of (i) 1D carbon based materials (carbon fibers, CNF, or nanotubes, CNT), (ii) 2D carbon materials (graphene, GO and rGO) and (iii) Fe_3O_4/Fe_2O_3 etc. has become a promising candidate for EMI shielding [33,40–43]. Shi et al. [33] fabricated Fe_3O_4/CNT/graphene composites via solvothermal and maximum reflection loss (RL) of −35.30 dB and bandwidth of 9.01 GHz with RL ≤ −10 dB with the coating layer thickness of 3.0 mm. Singh et al. [40] have reported the synthesis of Fe_3O_4/CNT/rGO sandwich network using large multi-step process and the resulting network demonstrates the shielding effectiveness value more than 37 dB (> 99.98% attenuation, in the range of 12.4–18 GHz). Zhang et al. [42] used a two-step synthesis method to fabricate 3D Fe_3O_4/CNT/rGO composites, with the maximum RL of −36 dB but bandwidth is only 3.60 GHz with thickness of 2.0 mm. These reported works show the great enhancement in properties after CNT/CNF inserting between graphene/rGO sheets linking the individual sheets to form an intertwined connected structure. Also it is believed that high electrical conductivity and connectivity of the conductive fillers (rGO and CNTs) can improve EMI shielding performance [44–46]. The above reported 3D architectures show that multi-step process and several approaches have been successfully used to synthesize 3D nanostructures. It should be noted however, that the adopted routes are rather complicated, time consuming and difficult to scale up.

In this work, we have synthesized 3D f-Fe_3O_4-VCNTs@rGO hybrid materials via GO reduction and exfoliation by microwave irradiation. The route is simple, opens way to large scale synthesis and fast processing (few seconds). The synthesized 3D f-Fe_3O_4-VCNTs@rGO hybrid materials have been used for EMI shielding. The f-Fe_3O_4 NPs on the tip of VCNTs grown on the surfaces of rGO NSs provide good combination of magnetic and dielectric losses, to achieve the desirable improvement of EMI shielding. Due to the synergistic effect between interfacial polarization and polarization relaxation, the obtained 3D f-Fe_3O_4-VCNTs@rGO hybrids exhibit excellent EMI shielding properties in the measured frequency range 8.2–12.4 GHz (X-band), which is the critical radar detection range.

2. Experimental section

2.1. Synthesis of graphite oxide and rGO NSs

Graphite oxide was synthesized by chemical oxidation of natural graphite powder, using the modified Staudenmaier's method [47]. Graphite powder (5 g) was continuously stirred with a mixture of H_2SO_4 (90 ml) and HNO_3 (45 ml) solution at room temperature. The solution container was placed into an ice-water bath to maintain constant temperature and $KClO_3$ (55 g) was slowly poured into the solution to avoid excess temperature rise due to exothermic reaction. This solution was continuously magnetic stirred for five days at room temperature for better oxidation of the graphite powder. The as obtained product was washed with DI water and further added with 10% HCl solution to remove sulphate and other ion impurities. It was then again washed several times with DI water until a pH of 7 was reached. Finally, graphite oxide powder was treated with microwave irradiation in oven (Consul-CMW30AB) (900 W for 1 min) for exfoliation and partial reduction into rGO. Some amount of graphite oxide powder was used in the next step for the synthesis of 3D f-Fe_3O_4-VCNTs@rGO hybrids.

2.2. Synthesis of 3D f-Fe_3O_4-VCNTs@rGO hybrids

The f-Fe_3O_4-VCNTs@rGO hybrids were synthesized according to the previous report [48]. In brief, 2.5 mg of ferrocene ($Fe(C_5H_5)_2$) were dispersed by sonication for 10 min in 200 mL C_2H_5OH and the suspension was magnetic stirred for 20 min, and then 1.5 g of graphite oxide were added to the suspension with vigorous magnetic stirring. Finally, the resulting black mixture product was heated (45 °C) for complete evaporation of C_2H_5OH. After that, the mixture was transferred into a quartz cup and then directly treated with microwave irradiation (Consul-CMW30AB) (900 W for 2 min) for the formation of 3D f-Fe_3O_4-VCNTs@rGO hybrids (faceted Fe_3O_4 NPs containing VCNTs@rGO NSs). For the formation of Fe_3O_4 NPs@rGO NSs, the mixture was treated with low microwave power (600 W for 1.5 min).

2.3. Characterization techniques

The crystal structures of the as synthesized materials (rGO NSs and 3D f-Fe_3O_4-VCNTs@rGO hybrids) were analyzed by powder X-ray diffraction (XRD- D/MAX-2500/PC; Rigaku Co., Tokyo, Japan) over 2θ range from 16 to 65°. The morphologies and microstructure of the as-prepared materials were characterized by field-emission scanning electron microscope (SEM- Dual Beam FIB/FEG model FEI Nova 200) equipped with energy dispersive X-ray spectroscopy (EDS). Raman measurements were carried out to determine the defect inside the hybrids material using a spectrometer with a 473 nm laser (NT-MDT NTEGRA Spectra). The X-ray photoelectron spectroscopy (XPS) spectrum was recorded using a SPECS system XR 50 X-ray source (Al K_α, 1486.6 eV) equipped Phoibos 150 hemispherical energy analyzer with MCD 9 detector. To study the thermal decomposition behaviour of the synthesized materials, a thermogravimetric analysis (TGA) was carried out using a differential scanning calorimetry (SDT-Q600, TA Instruments). The TG instrument was set to heat up the sample in air

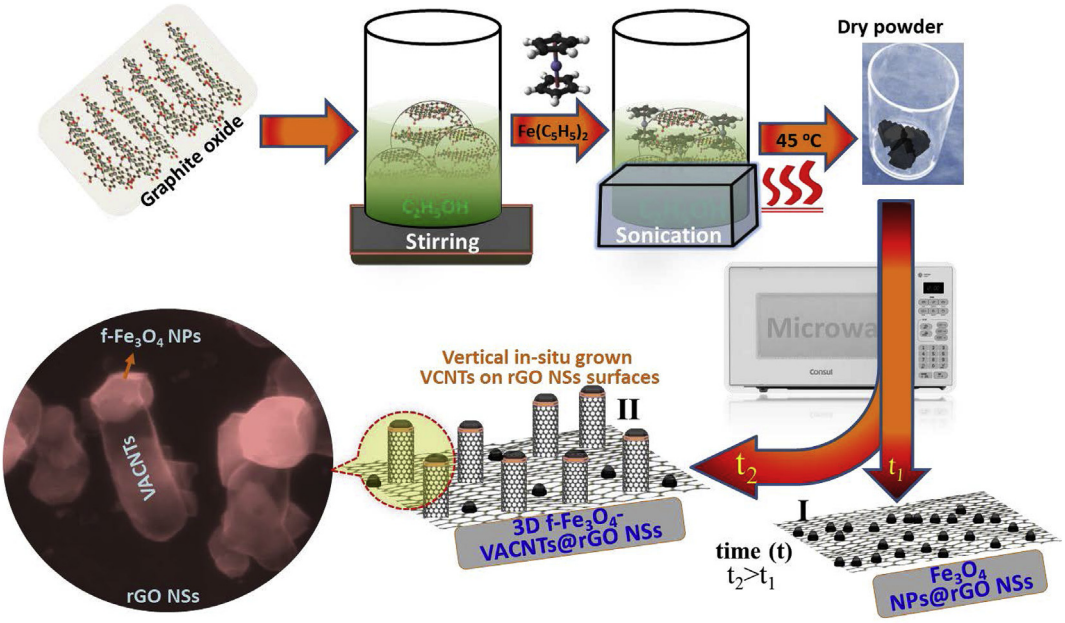

Fig. 1. Schematic representation for the synthesis of Fe_3O_4 NPs@rGO NSs and 3D f-Fe_3O_4-VCNTs@rGO hybrids.

from room temperature to 850 °C at a constant ramp rate of 10 °C/min. EMI shielding measurements were carried out using Agilent E8362B Vector Network Analyzer in the frequency range of 8.2–12.4 GHz (X band). Samples for EMI measurements were prepared by making pellets of the powder samples of dimensions 15 mm × 8 mm with 1 mm thickness by hydraulic pressure (10 ton pressure). The prepared thin pellets were kept in Cu sample holder and sandwiched between two ports network analyzer.

3. Results and discussion

3.1. Morphological and structural characterization

The schematic for the synthesis of 3D f-Fe_3O_4-VCNTs@rGO hybrids is illustrated in Fig. 1. The proposed mechanism involved several steps. Initially when the graphite oxide dispersion was added to $Fe(C_5H_5)_2$, the $Fe(C_5H_5)_2$ spreads on the surface of the graphite oxide. During the microwave radiation, $Fe(C_5H_5)_2$ are dissociated and decomposed into Fe containing NPs and graphite oxide transforms into rGO NSs (step-I) [48,49]. During continued microwave irradiation, the dissociated Fe NPs start to work as tip growth catalysts for the growth of VCNTs utilizing additional carbon from rGO (see description of the detailed mechanism below). But for longer microwave irradiation, the Fe NPs can be oxidized and transformed into f-Fe_3O_4 NPs thus terminating the growth of VCNTs resulting in only few hundred nanometers long nanotubes (step-II). This 3D interconnected and porous networked structure of 3D f-Fe_3O_4-VCNTs@rGO hybrids beneficiate EMI shielding by helping EM wave to absorb inside the materials.

The surface morphologies of as synthesized rGO NSs were investigated by SEM as shown in typical SEM images with different magnifications (Fig. 2). SEM images show that rGO NSs are oriented randomly and are wrinkled on their surfaces. The lamella structure of wrinkled rGO NSs is due to the van der Waals interactions. The as synthesized rGO NSs contain highly porous nanostructures with high surface area.

Fig. 3a show the SEM image of the Fe_3O_4 NPs@rGO NSs at low magnifications. The SEM images of Fe_3O_4 NPs@rGO NSs reveal the anchored Fe_3O_4 NPs on the surfaces of rGO NSs with diameter less than 1 μm, appearing as bright white spots distributed on the rGO NSs. The SEM image reveals that the Fe_3O_4 NPs are attached to rGO NSs and uniformly covers the rGO NSs. The high-magnification image in Fig. 3b, shows that the Fe_3O_4 NPs have nearly spherical shapes and are well attached to the surfaces of rGO NSs.

Typical morphologies of hierarchical 3D f-Fe_3O_4-VCNTs@rGO hybrids are shown in Fig. 4. SEM observation reveals the structures that VCNTs are embedded widely and grown uniformly on the rGO NSs surfaces (Fig. 4a). Also the images show the free-standing aligned VCNTs on the surfaces of rGO NSs. High resolution SEM images confirmed the co-existence of VCNTs and rGO NSs with the diameter of VCNTs in the range 150–170 nm and with vertical length of 300–450 nm (Fig. 4f). The VCNTs are grown on rGO surfaces without branching. The mechanism behind the growth of VCNTs on rGO with the assistance of $Fe(C_5H_5)_2$ is already discussed above.

The crystalline nature of the as-synthesized hierarchical 3D f-Fe_3O_4-VCNTs@rGO hybrids was examined by XRD analysis (Fig. 5a). The diffraction peaks for 3D f-Fe_3O_4-VCNTs@rGO at 2θ = 30.3, 35.4, 37.1, 43.3, 53.6, 57.2, and 62.9° can be assigned to (220), (311), (222), (400), (422), (511) and (440) diffraction peaks, respectively for Fe_3O_4 (JCPDS No. 72–2303) [18]. The inset of Fig. 5a, shows the X-ray diffraction pattern for rGO NSs reveals a broadened peak centered at 2θ = 25.7, corresponding to d_{002} spacing, characteristic for rGO NSs (Inset: Fig. 5a). As for 3D f-Fe_3O_4-VCNTs@rGO hybrids, all the characteristic peaks of Fe_3O_4 NPs and rGO NSs are observed, demonstrating the coexistence of Fe_3O_4 and rGO NSs in the hybrid networks.

The EDS of hierarchical 3D f-Fe_3O_4-VCNTs@rGO hybrids is shown in Fig. 5b, and the C, O and Fe content were 80.91 wt%, 10.77 wt% and 8.32 wt%, respectively. Inset of Fig. 5b shows the EDS of rGO NSs deducing the elemental contents as C (92.57 wt%) and O (7.43 wt%). The elemental concentration as obtained from EDS in rGO NSs and 3D f-Fe_3O_4-VCNTs@rGO hybrids have been shown in inset of Fig. 5b.

Raman spectroscopy is the powerful technique widely used to for characterizing microstructure for obtaining structural defects and disorder information especially for carbon-based materials [50,51]. The defective structure of the rGO NSs and hierarchical 3D f-Fe_3O_4-VCNTs@rGO hybrids were investigated by Raman spectroscopy as shown in Fig. 5c. Typical peaks of as-synthesized rGO NSs and 3D f-Fe_3O_4-VCNTs@rGO hybrids materials are centered at 1372 and 1596 cm^{-1} called as D band and G band, respectively. The D band is associated with structural defects and partially disordered structures of the sp^2 domains [52]. Similarly, the G band is related to the E_{2g} vibration mode

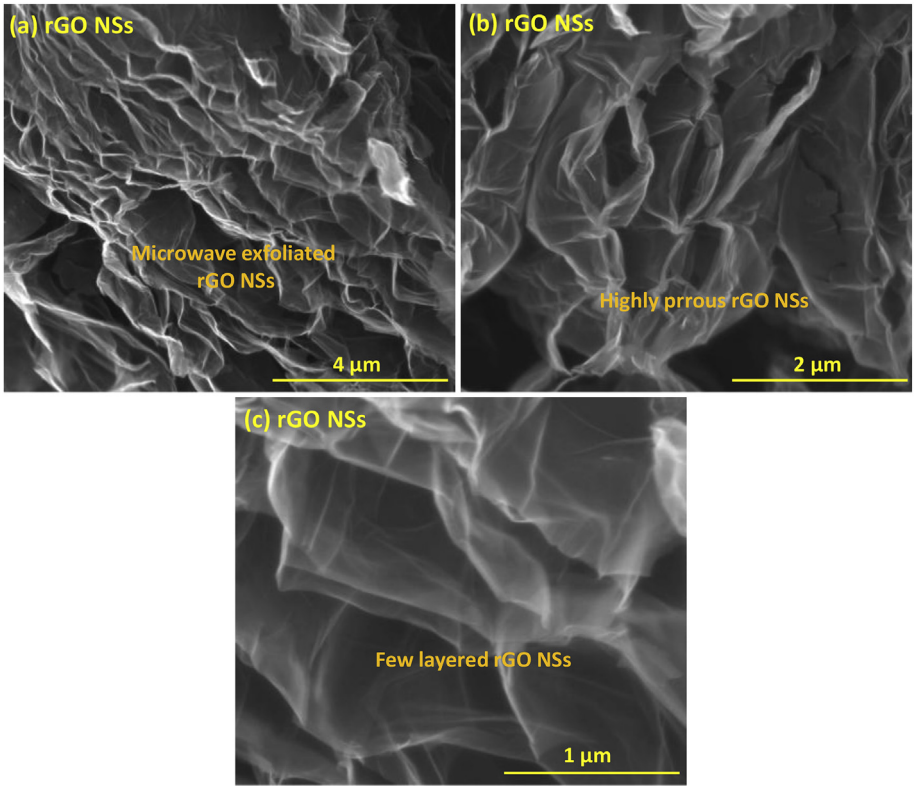

Fig. 2. SEM images of rGO NSs at different magnifications.

of sp^2 carbon domains which is usually used to explain the degree of graphitization [53]. In general, the higher intensity of D band compared to that of G band indicates a higher disorder in graphene materials and the intensity ratio of D and G peak (I_D/I_G) reflects the defects density of graphene based materials. As shown in Fig. 5c, the I_D/I_G of rGO NSs is 0.48, however, the I_D/I_G of 3D f-Fe_3O_4-VCNTs@rGO hybrids is increased to 0.98, indicating that the growth of VCNTs on the surfaces of rGO NSs generates structural defects in rGO NSs [54,55].

To evaluate the content of Fe_3O_4 NPs in hierarchical 3D f-Fe_3O_4-VCNTs@rGO hybrids, TGA characterization of rGO NSs and 3D f-Fe_3O_4-VCNTs@rGO hybrids were carried out in air as shown in Fig. 5d. It explains the strong interaction between Fe_3O_4 NPs and rGO NSs. The TGA curve of rGO NSs and 3D f-Fe_3O_4-VCNTs@rGO hybrids can be divided into two sections according to weight loss for both samples with increase in temperature. The small weight loss starts at the temperature < 470 °C for the first stage and sharp weight loss appears in the temperature range of 470–650 °C for the second stage. The rGO NSs and 3D f-Fe_3O_4-VCNTs@rGO hybrids show gradual weight loss of 12 wt.% and 5 wt.%, respectively from room temperature to 470 °C. This weight loss in this temperature range are mainly due to the evaporation of the absorbed water, removal of oxygen-containing functional groups and some oxidation of rGO NSs [56]. The sharp weight loss occurs in the temperature range of 470–650 °C for rGO NSs and 3D f-Fe_3O_4-VCNTs@rGO hybrids [57]. At 650 °C, the negligible remaining weight of rGO NSs were lower than 0.5 wt.%. The weight loss of 3D f-Fe_3O_4-VCNTs@rGO hybrids were stabilized at 58 wt.% above 650 °C, indicating complete removal of rGO NSs and remaining ~42 wt.% of Fe_3O_4 NPs present in the 3D f-Fe_3O_4-VCNTs@rGO hybrids [58,59]. The result implies that the weight fraction of Fe_3O_4 NPs in 3D f-Fe_3O_4-VCNTs@rGO hybrids were ~42 wt.% based on the assumptions that the weight loss is due to the complete combustion of rGO and Fe_3O_4 NPs are fully oxidized to Fe_2O_3 NPs [60,61]. This means that the combination of rGO NSs with Fe_3O_4 NPs provides more thermal stability, implying a strong interaction between rGO NSs and Fe_3O_4 NPs [58]. The weight losses at higher temperature range (> 470 °C) are due to oxidation in air, continuous decomposition of more stable carbon in rGO NSs and

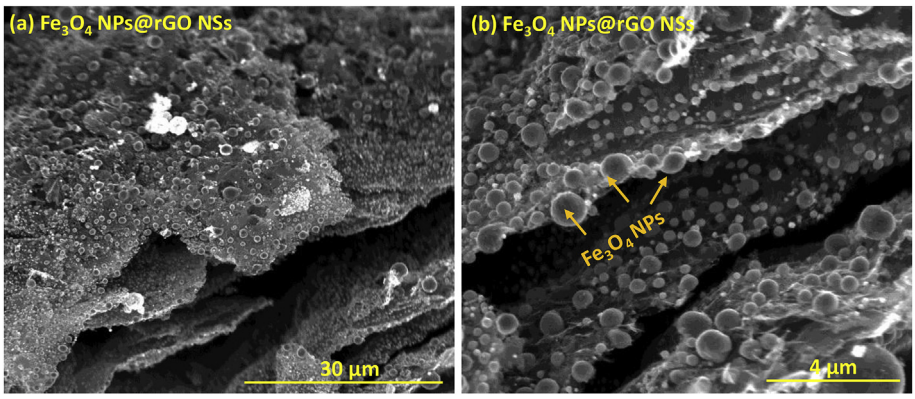

Fig. 3. SEM images of Fe_3O_4 NPs@rGO NSs at different magnifications.

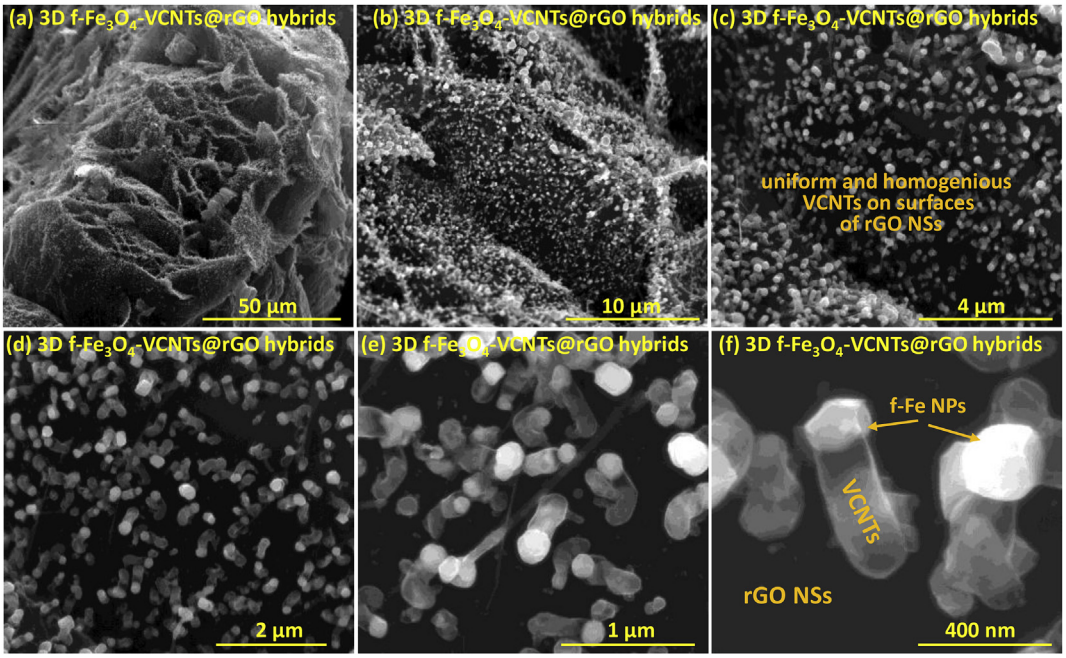

Fig. 4. SEM images of hierarchical 3D f-Fe_3O_4-VCNTs@rGO hybrids at different magnifications.

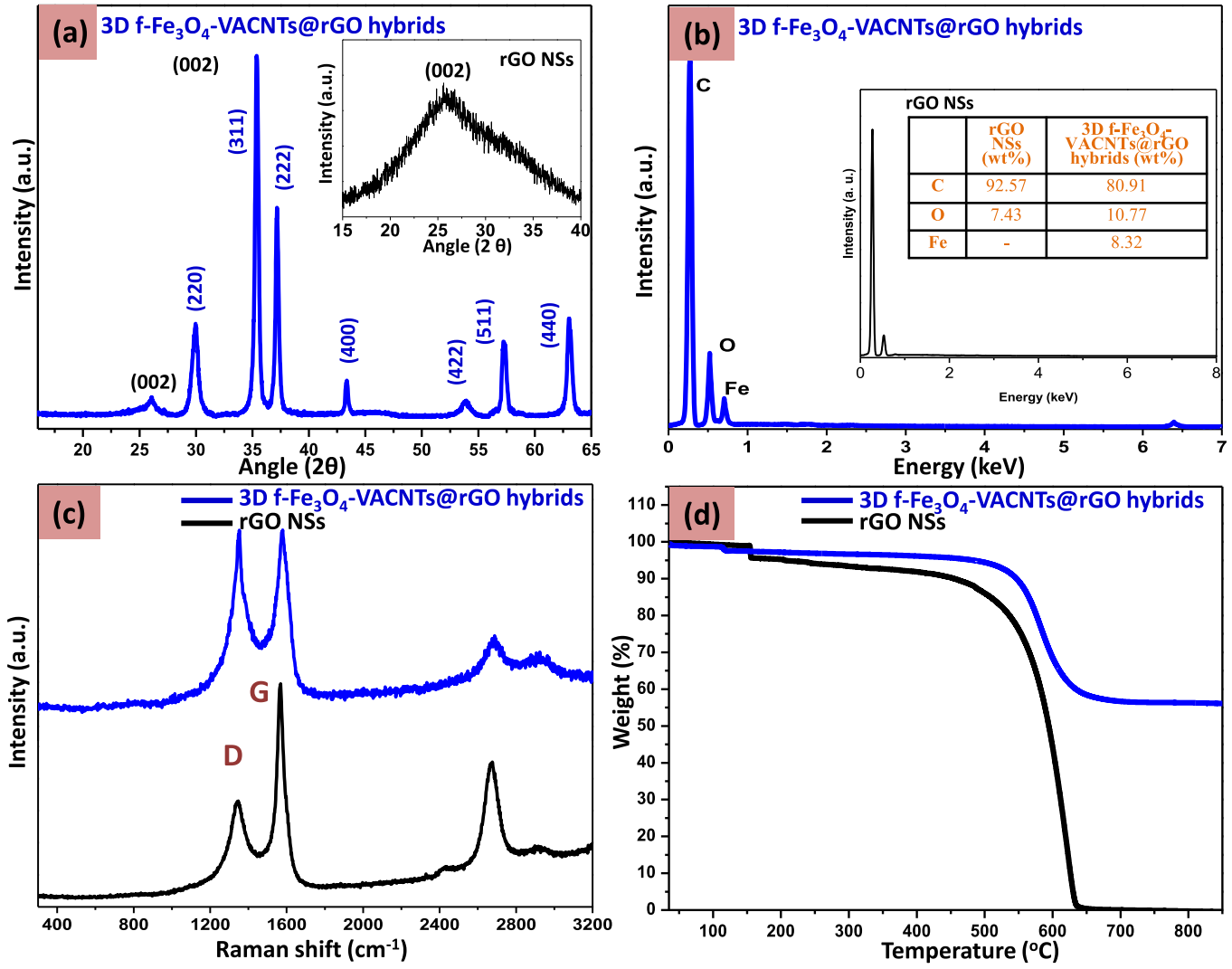

Fig. 5. (a) X-ray diffraction, (b) EDS pattern, (c) Raman spectra and (d) TGA of rGO NSs and hierarchical 3D f-Fe_3O_4-VCNTs@rGO hybrids.

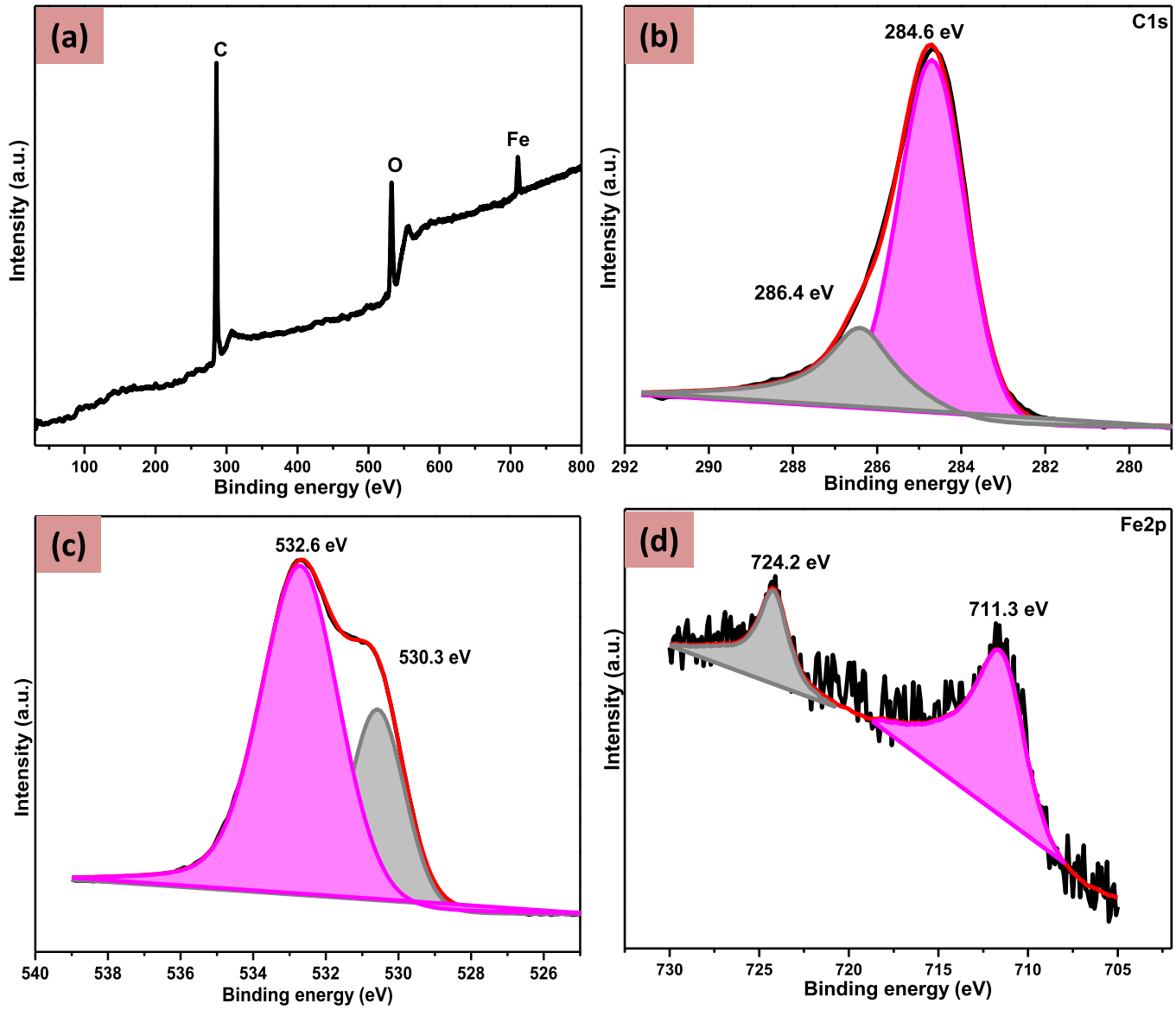

Fig. 6. XPS spectra of hierarchical 3D f-Fe_3O_4-VCNTs@rGO NSs hybrids. (a) Complete survey, (b) C 1s spectra (c) O spectra and (d) Fe 2p spectra.

combustion of rGO NSs skeleton in air [62].

XPS investigation was carried out to determine the chemical and electronic state of the elements in hierarchical 3D f-Fe_3O_4-VCNTs@rGO hybrids (Fig. 6). The signals C, O and Fe were evidenced at ~284, ~532 and ~724 eV as shown in Fig. 6a, which reveals that the hybrids consists of these three major elements. Among the signals, C1s peak which appears due to rGO NSs and VCNTs are prominent in Fig. 6a. As shown in Fig. 6b, the deconvoluted peaks of C 1s spectrum of 3D f-Fe_3O_4-VCNTs@rGO hybrids can be fitted with two component peaks at 284.6 and 286.4 eV, corresponding to C—C/C=C (284.6 eV) in the aromatic rings and C—O (286.4 eV) of epoxy groups, respectively [63,64]. In Fig. 6c, deconvoluted peak of O 1s spectrum shows two split peaks resulting from the different chemical bonding states of oxygen element in 3D f-Fe_3O_4-VCNTs@rGO hybrids. The peaks located at 530.3 and 532.6 eV, are attributed to oxygen in the lattice (Fe—O) [65], and oxygen in the lattice (C—O), respectively [64,66]. The Fe 2p XPS spectrum of the 3D f-Fe_3O_4-VCNTs@rGO hybrids exhibit two peaks at 711.3 and 724.2 eV corresponding to the Fe $2p_{3/2}$ and Fe $2p_{1/2}$ spin orbit peaks of Fe_3O_4 (Fig. 6d), confirming formation of 3D f-Fe_3O_4-VCNTs@rGO hybrids [67,68]. The absence of the characteristics satellite peaks in the XPS also confirms the formation of Fe_3O_4 rather than Fe_2O_3 [69,70].

During microwave irradiation for the formation of hierarchical 3D f-Fe_3O_4-VCNTs@rGO hybrids, in the presence of air, the graphite oxide carbonaceous chemicals could be combusted and some gases blown out. In this process, a significant amount of heat might be released, and the local temperatures of the sample might be higher than the average material temperature. During the microwave irradiation, in situ thermal reduction and exfoliation of graphite oxide to rGO NSs and thermal decomposition of $Fe(C_5H_5)_2$ to Fe NPs occurs at same time during reaction processing [71]. It is known that partially reduced rGO NSs have some functional groups such as epoxy, hydroxyl, carbocyclic and carboxyl on its surface and edges that become negatively charged. The positive Fe metal ions in the system can be attached to the surface and interact with the functional groups via electrostatic attraction and serve as nucleation precursors. In our case, Fe ions in this process tend to attach to some particular positions of the rGO NSs surfaces with functional group, creating the centers of nucleation of Fe NPs, eventually resulting in decoration of rGO NSs surfaces by Fe NPs at the initial stage of microwave irradiation. At some higher microwave irradiation reaction time the decorated Fe NPs act as catalyst for the growth of VCNTs [72]. The nano-sized Fe NPs catalyst starts to dissolve carbon

from rGO NSs at higher temperatures. Further, the supersaturation of NPs with carbon atoms is achieved after so called incubation time that can extend for several tens of seconds [73], and the process of nanotubes formation following the tip growth mechanism can be initiated. However, as the main source of carbon atoms is the underlying surface of rGO, the nanotube growth tends to slow down or even terminate soon after detachment of the Fe particles from the surface. As the result, only short nanotubes can be grown in this process. At longer microwave irradiation time, Fe NPs attached at the tip of VCNTs transform into Fe_3O_4 NPs due to continuous oxidation in air. Note that further increase of the irradiation time can result in gradual burning of nanotubes in air.

3.2. Electromagnetic interference shielding

The EMI-SE is the ability to shield devices from the EM microwave source and is expressed as a logarithmic ratio of the incident and transmitted power [74].

$$SE(dB) = 10\log\frac{P_T}{P_I} \tag{1}$$

Where P_T and P_I are the incident and transmitted power components of the EM microwave, respectively. For shielding materials, total EMI-SE (SE_T) consists of SE due to absorption (SE_A), reflection (SE_R) and multiple reflection (SE_M) components. So, total SE (SE_T) can be written as by addition of all these as [75].

$$SE_T = SE_A + SE_R + SE_M \tag{2}$$

The component SE_A term is associated with the energy loss associated with the current induced in the shielding material whereas SE_R relates with the impedance mismatching between the free spaces and shielding material. SE_M occurs between the two interfaces and is usually ignored when the SE_T value increases beyond 10 dB [76]. Also, according to Schel-Kunoff's theory, multiple reflections can be neglected when the thickness (t) of the shielding material is greater than the skin depth (δ) (t > δ). The contribution from multiple internal reflections is merged in the absorption, as the re-reflected waves are absorbed or dissipated in the form of heat [77].

In two port network, S-parameters (scattering parameters) S_{11} (S_{22}), S_{12} (S_{21}) represents the transmission (T) and the reflection (R) coefficients given as

$$T = \left|\frac{E_T}{E_I}\right|^2 = |S_{12}|^2 = |S_{21}|^2 \tag{3}$$

$$R = \left|\frac{E_R}{E_I}\right|^2 = |S_{11}|^2 = |S_{22}|^2 \tag{4}$$

and the absorption coefficient (A) = 1- (R + T).

If the effect of multiple reflections between both interfaces of the material is negligible, then the relative intensity of the effectively incident electromagnetic wave inside the material after reflection is based on the quantity (1-R). Therefore, the effective absorbance (A_{eff}) can be written as with respect to the power of the effective incident electromagnetic wave inside the shielding material.

$$A_{eff} = \left(\frac{1-R-T}{1-R}\right) \tag{5}$$

The values of SE_A and SE_R can be written in form of R and T as [75].

$$SE_R = 10\log\left(\frac{1}{1-R}\right) \tag{6}$$

$$SE_A = 10\log\left(\frac{1}{1-A_{eff}}\right) = 10\log\left(\frac{1-R}{T}\right) \tag{7}$$

Putting the values of R and T in term of $|S_{21}|^2$ and $|S_{11}|^2$ from equations (3) and (4) in equations (6) and (7)

$$SE_R = 10\log\left(\frac{1}{1-|S_{11}|^2}\right) \tag{8}$$

$$SE_A = 10\log\left(\frac{1-|S_{11}|^2}{|S_{21}|^2}\right) \tag{9}$$

So, SE_T can be deduced from eqns. (8) and (9) as

$$SE_T = SE_R + SE_A = 20\log(S_{21}) \tag{10}$$

Electrical conductivity contributes in both the reflection and absorption parts. In the case of absorption, the EM microwave attenuates exponentially in the form of ohmic losses, heating up the material. The penetrating distance at which the strength of the wave is diminished to 1/e times the original value in the shielding material is defined as the skin depth δ. Using EM theory, we calculated the SE due to reflection (SE_R) and absorption (SE_A) as follows [78].

$$SE_R(dB) \approx 10\log\left(\frac{\sigma_{ac}}{16\omega\varepsilon_0\mu_r}\right) \tag{11}$$

$$SE_A(dB) = 20\left(\frac{t}{\delta}\right)\log_e = 8.68\left(\frac{t}{\delta}\right) = 8.68t\sqrt{\frac{\mu_r\omega\sigma_{ac}}{2}} \tag{12}$$

$$\delta = 8.68\left(\frac{t}{SE_A}\right) \tag{13}$$

where, σ_{ac} depends on the dielectric behaviour ($\sigma_{ac} = \omega\varepsilon_0\varepsilon''$) of the material, ω is the angular frequency (ω= 2πf), ε_0 is the free space permittivity, and μ_r is the relative magnetic permeability of the sample. Eqs. (11) and (12) reveal that with the increase in angular frequency(ω), the SE_R value decreases and SE_A increases.

Fig. 7a shows the SE_R for as synthesized samples. The analysis of obtained results shows that EMI SE_R for hierarchical 3D f-Fe_3O_4-VCNTs@rGO hybrids is lower as compared to Fe_3O_4 NPs@rGO NSs. The EMI SE_R for 3D f-Fe_3O_4-VCNTs@rGO hybrids is also lower than rGO NSs at higher frequency (> 9 GHz). The SEr for Fe_3O_4 NPs@rGO NSs and rGO were found similar near middle frequency range (10–10.5 GHz) and not significantly differ above 10.5 GHz. Fig. 7b shows the EMI SE_A for 3D f-Fe_3O_4-VCNTs@rGO hybrids, Fe_3O_4 NPs@rGO NSs and rGO having values 24.5, 11.5 and 8.0 dB (at 8.5 GHz), respectively. The EMI SE_A for rGO NSs is highly stable for the whole X band but slightly decreases in 3D f-Fe_3O_4-VCNTs@rGO hybrids at higher frequency from 24.5 (8.5 GHz) to 23.5 dB (12.4 GHz). The study of the reflection and absorption parts of shielding for 3D f-Fe_3O_4-VCNTs@rGO hybrids indicate absorption as the major shielding mechanism (Fig. 7a and b). Fig. 7c shows that the values of EMI SE_T for 3D f-Fe_3O_4-VCNTs@rGO hybrids, Fe_3O_4 NPs@rGO NSs and rGO are 26.7, 14.5 and 9.6 dB at 8.5 GHz. It represents that EMI SE_T for 3D f-Fe_3O_4-VCNTs@rGO hybrids is nearly 1.84 times higher as compared to Fe_3O_4 NPs@rGO NSs at 8.5 GHz. As compared to rGO NSs and Fe_3O_4 NPs@rGO NSs, the 3D f-Fe_3O_4-VCNTs@rGO hybrids revealed an increase in EMI SE_T due to the in-situ growth of VCNTs with help of Fe_3O_4 NPs. Therefore, it is expected that the use of rGO NSs and VCNTs containing Fe_3O_4 NPs in 3D f-Fe_3O_4-VCNTs@rGO hybrids with high aspect ratio and conductivity could possibly results as promising EMI shielding value. The adopted microwave approach for synthesis of 3D f-Fe_3O_4-VCNTs@rGO hybrids is fast (few min) and very simple approach to other reported works in literature as listed in Table 1. The obtained EMI SE value of 23 dB, which is superior to most of the EMI SE materials reported in previous literature using various carbon based hybrids/composites (Table 1).

A strong skin effect was observed in 3D f-Fe_3O_4-VCNTs@rGO hybrids as compared to Fe_3O_4 NPs@rGO NSs and rGO NSs, due to the presence of VCNTs on the surfaces of rGO NSs. Fig. 7d shows the skin depth for rGO NSs, Fe_3O_4 NPs@rGO NSs and 3D f-Fe_3O_4-VCNTs@rGO hybrids as ~1.09 mm, ~0.76 mm and ~0.34 mm, respectively. The in-situ growth of VCNTs with help of Fe NPs on rGO NSs reduces the skin

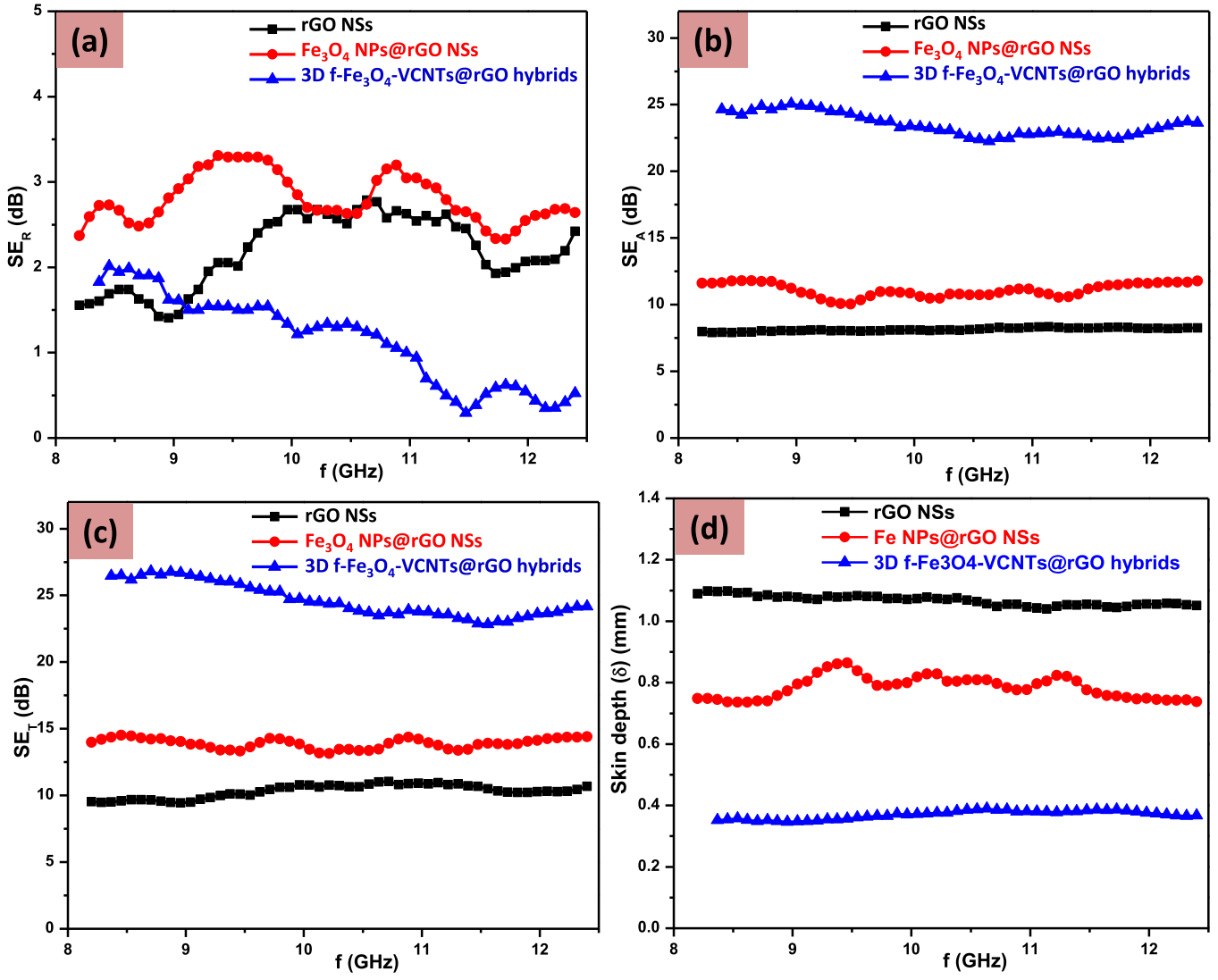

Fig. 7. EMI-SE and skin depth of rGO NSs, Fe_3O_4 NPs@rGO NSs and hierarchical 3D f-Fe_3O_4-VCNTs@rGO hybrids. (a) SE_R, (b) SE_A, (c) SE_T, and (d) skin depth (δ) in frequency range of 8.2–12.4 GHz (X-band).

Table 1
EMI SE comparison of representative work used for various carbon based hybrids/composites by different route including synthesis timing.

S. No	Method/technique (Time taken)	Carbon containing hybrids/composites[a]	Thickness (mm)	Frequency range (GHz)	EMI SE (dB)	Ref.
1.	Co-precipitation route (5–30 min)	3D Fe_3O_4-MWCNTs	1.5	4.1	23	[38]
2.	Hot-pressing process (> 1 h)	MWNT/PS foam composite (7 wt %)	–	8.2–12.4	20	[44]
3.	Subcritical CO_2 foaming technique (> 24 h)	graphene/PMMA foam	2.4	8–12	13–19	[45]
4.	Melt-mixing technique (~3 h)	MWCNT/EMA nanocomposites	5.0	8.2–12.4	22	[79]
5.	Solvent cast Method (8 h)	MWCNT/PVDF/Au composite (1 wt% Au NPs)	0.5	8–12	23.0	[80]
6.	Supercritical CO_2 foaming technique (~48 h)	MWCNTs/Fe_3O_4/PMMA nanocomposite	2.5	8–12	13.1	[81]
7.	Solution process (~2 h)	rGO/epoxy composite (15 wt%)	0.8–1.1	8.2–12.4	21	[82]
8.	Melt compound (~3 h)	graphene/PC nanocomposites	2.0	8–13	15	[83]
9.	Freeze-drying processes composites (0.2 wt%) (6 h)	graphene aerogels/epoxy	4.0	8–12	25	[84]
10.	Phase separation method (> 24 h)	graphene/PEI/Fe_3O_4 composite (10 wt %)	2.5	8–12	16	[85]
11.	Solvothermal method (~12 h)	rGO/Fe_3O_4/paraffin wax composite	2.0	12.9	24	[86]
12.	Solvothermal self-assembly method (> 12 h)	graphene/MWCNT foam	2.0	4–12	22.7	[87]
13.	Microwave method (2 min)	3D f-Fe_3O_4-VCNTs@rGO hybrids	1.0	8.2–12.4	25	This work

[a] PS: polystyrene; EMA: ethylene methyl acrylate; PVDF: Polyvinylidene fluoride; PMMA: poly (methyl methacrylate); PC: Polycarbonate; PEI: Polyethylenimine.

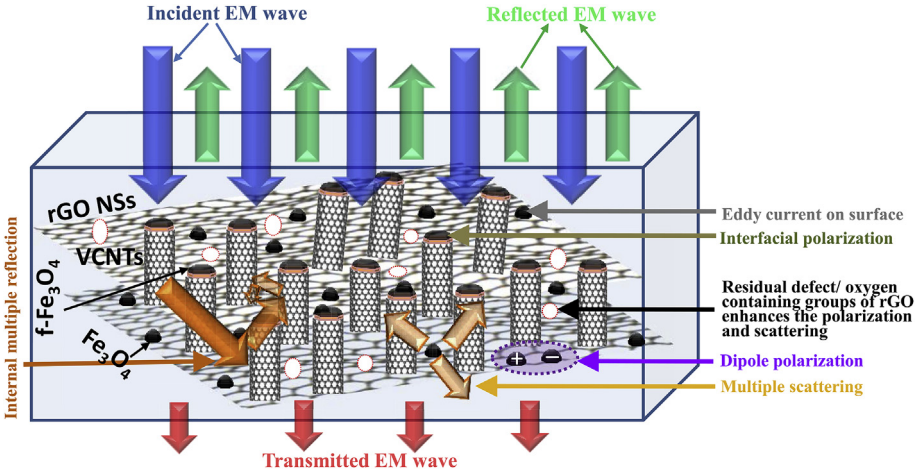

Fig. 8. Schematic representation of EM microwave absorption in the hierarchical 3D f-Fe_3O_4-VCNTs@rGO hybrids.

depth value and hence prevents the penetration of EMI wave to larger depth inside the 3D f-Fe_3O_4-VCNTs@rGO hybrids. Our analysis reveals that the skin depth in 3D f-Fe_3O_4-VCNTs@rGO hybrids is very low as compared to rGO NSs. Thus, as synthesized 3D f-Fe_3O_4-VCNTs@rGO hybrids are good materials for EMI shielding.

The proposed interaction of EM radiation with hierarchical 3D f-Fe_3O_4-VCNTs@rGO hybrids is shown in Fig. 8 through a schematic representation. Fig. 8 shows the responsible mechanism for EM microwave absorption inside the as synthesized 3D f-Fe_3O_4-VCNTs@rGO hybrids. Thus the maximum SE_T achieved for the 3D f-Fe_3O_4-VCNTs@rGO hybrids which represents improved microwave shielding can be ascribed to the VCNTs containing Fe_3O_4 NPs attached with rGO NSs surfaces. The assembly of f-Fe_3O_4, VCNTs and rGO NSs are believed to increase the geometrical effect and consequently enhanced shielding effectiveness. Furthermore, VCNTs in 3D f-Fe_3O_4-VCNTs@rGO hybrids offer higher defect density in comparison to the Fe_3O_4 NPs@rGO NSs and rGO NSs. The VCNTs on rGO NSs in 3D f-Fe_3O_4-VCNTs@rGO hybrids are also aligned in a specific direction and helps in maximizing the attenuation of an EM microwave radiation. In other words, 1D VCNTs nanostructure on 2D rGO NSs appears to be good candidates for microwave shielding. In the hybrid materials, shielding effectiveness is the result of magnetic and dielectric loss due to the interaction of materials with EM microwave. Magnetic loss is due to eddy current produced, natural resonance and anisotropy energy present in the hybrids, as in the microwave X-band range, the presence of f-Fe_3O_4 NPs with VCNTs in the hybrids causes the eddy current [81]. The Fe_3O_4 with aligned VCNTs would help to prevent the skin effect and shows strong ability to absorb EM microwave through natural resonance, eddy current and hysteresis losses [88–91]. The VCNTs with f-Fe_3O_4 on rGO NSs introduces interfaces and more polarization charges at the surface [92]. Also, the induced defects and functional groups on the rGO NSs increase the absorption of the microwave [90,93,94]. The high conductivity of porous rGO plays the main role in EM microwave attenuation and prevent the EM microwave to penetrate the hybrids materials [92]. From all the above mentioned discussion, it is concluded that VCNTs containing Fe_3O_4 attached with rGO NSs are capable aspirants as versatile and lightweight shielding materials against EM radiations.

4. Conclusion

In summary, we have synthesized hierarchical 3D f-Fe_3O_4-VCNTs@rGO NSs hybrids material by using simple microwave approach for the application of EMI shielding. The as synthesized hybrids material clearly demonstrate that in-situ growth of VCNTs with help of Fe NPs on the surfaces of rGO NSs favours creation of an excellent EM absorber. The 3D f-Fe_3O_4-VCNTs@rGO hybrids contain VCNTs on high quality porous rGO NSs with large surface area. The 3D f-Fe_3O_4-VCNTs@rGO hybrids show higher EMI shielding values as compared to pristine rGO NSs. The VCNTs on rGO surfaces have a pronounced impact on the EMI shielding properties and exhibit enhanced shielding effectiveness and shows nearly ~25 dB at 1.0 mm thickness of 3D f-Fe_3O_4-VCNTs@rGO hybrids film in frequency region of 8.2–12.4 GHz. The obtained results suggest that the systems are promising EMI absorption materials in the microwave X-band frequency range. On account of the simple, fast and low cost preparation process, the synthesized 3D f-Fe_3O_4-VCNTs@rGO hybrids can be used as good cladding wave-absorbing materials. The high EMI shielding effectiveness and thermal stable behaviour of 3D f-Fe_3O_4-VCNTs@rGO hybrids useful for EMI shielding applications particularly in aerospace and aviation research areas.

Acknowledgements

The author (R. Kumar) acknowledges Japan Society for the Promotion of Science (Standard) for international/foreign postdoctoral fellowship (P18063) and JSPS KAKENHI Grant No. 18F18063 (financial support). AVA and SAM would like to acknowledge CNPq and FAPESP (Brazil) for financial support.

References

[1] Fang S, Huang D, Lv R, Bai Y, Huang Z-H, Gu J, et al. Three-dimensional reduced graphene oxide powder for efficient microwave absorption in the S-band (2-4 GHz). RSC Adv 2017;7(41):25773–9.
[2] Song W-L, Fan L-Z, Hou Z-L, Zhang K-L, Ma Y, Cao M-S. A wearable microwave absorption cloth. J Mater Chem C 2017;5(9):2432–41.
[3] Lu L, Xing D, Teh KS, Liu H, Xie Y, Liu X, et al. Structural effects in a composite nonwoven fabric on EMI shielding. Mater Des 2017;120:354–62.
[4] Mishra M, Singh AP, Gupta V, Chandra A, Dhawan SK. Tunable EMI shielding effectiveness using new exotic carbon: polymer composites. J Alloy Comp 2016;688:399–403.
[5] Zhang Y, Huang Y, Zhang T, Chang H, Xiao P, Chen H, et al. Broadband and tunable high-performance microwave absorption of an ultralight and highly compressible graphene foam. Adv Mater 2015;27(12):2049–53.
[6] Sun H, Che R, You X, Jiang Y, Yang Z, Deng J, et al. Cross-stacking aligned carbon-nanotube films to tune microwave absorption frequencies and increase absorption intensities. Adv Mater 2014;26(48):8120–5.
[7] Singh AK, Shishkin A, Koppel T, Gupta N. A review of porous lightweight composite materials for electromagnetic interference shielding. Compos B Eng 2018;149:188–97.
[8] Tang W, Lu L, Xing D, Fang H, Liu Q, Teh KS. A carbon-fabric/polycarbonate sandwiched film with high tensile and EMI shielding comprehensive properties: an experimental study. Compos B Eng 2018;152:8–16.
[9] Chaudhary A, Kumari S, Kumar R, Teotia S, Singh BP, Singh AP, et al. Lightweight and easily foldable MCMB-MWCNTs composite paper with exceptional electromagnetic interference shielding. ACS Appl Mater Interfaces 2016;8(16):10600–8.
[10] Tzeng S-S, Chang F-Y. EMI shielding effectiveness of metal-coated carbon fiber-reinforced ABS composites. Mater Sci Eng, A 2001;302(2):258–67.
[11] Kim MS, Kim HK, Byun SW, Jeong SH, Hong YK, Joo JS, et al. PET fabric/polypyrrole composite with high electrical conductivity for EMI shielding. Synth Met

2002;126(2–3):233–9.
[12] Thomassin J-M, Jérôme C, Pardoen T, Bailly C, Huynen I, Detrembleur C. Polymer/carbon based composites as electromagnetic interference (EMI) shielding materials. Mater Sci Eng R Rep 2013;74(7):211–32.
[13] Zheng J, Lv H, Lin X, Ji G, Li X, Du Y. Enhanced microwave electromagnetic properties of Fe_3O_4/graphene nanosheet composites. J Alloy Comp 2014;589:174–81.
[14] Zhu M, Dong Y, Xiao B, Du Y, Yang P, Wang X. Enhanced photocatalytic hydrogen evolution performance based on Ru-trisdicarboxybipyridine-reduced graphene oxide hybrid. J Mater Chem 2012;22(45):23773–9.
[15] Hou Z-L, Zhou H-F, Kong L-B, Jin H-B, Qi X, Cao M-S. Enhanced ferromagnetism and microwave absorption properties of BiFeO3 nanocrystals with Ho substitution. Mater Lett 2012;84:110–3.
[16] Kumar R, Singh R, Singh D. Synthesis strategies for graphene. Graphene science handbook. CRC Press; 2016. p. 73–114.
[17] Geim AK. Graphene: status and prospects. Science 2009;324(5934):1530–4.
[18] Kumar R, Singh RK, Singh DP, Joanni E, Yadav RM, Moshkalev SA. Laser-assisted synthesis, reduction and micro-patterning of graphene: recent progress and applications. Coord Chem Rev 2017;342:34–79.
[19] Wu J, Chen J, Zhao Y, Liu W, Zhang W. Effect of electrophoretic condition on the electromagnetic interference shielding performance of reduced graphene oxide-carbon fiber/epoxy resin composites. Compos B Eng 2016;105:167–75.
[20] Kumar R, Joanni E, Singh RK, Singh DP, Moshkalev SA. Recent advances in the synthesis and modification of carbon-based 2D materials for application in energy conversion and storage. Prog Energy Combust Sci 2018;67:115–57.
[21] Gholampoor M, Movassagh-Alanagh F, Salimkhani H. Fabrication of nano-Fe_3O_4 3D structure on carbon fibers as a microwave absorber and EMI shielding composite by modified EPD method. Solid State Sci 2017;64:51–61.
[22] Xu L, Zhang B, Chen Y, Neoh K-G, Kang E-T. Graphene-polymer nanocomposites: preparation, characterization, and applications. Graphene science handbook. CRC Press; 2016. p. 493–524.
[23] Singh RK, Kumar R, Singh DP. Graphene oxide: strategies for synthesis, reduction and frontier applications. RSC Adv 2016;6(69):64993–5011.
[24] Georgakilas V, Tiwari JN, Kemp KC, Perman JA, Bourlinos AB, Kim KS, et al. Noncovalent functionalization of graphene and graphene oxide for energy materials, biosensing, catalytic, and biomedical applications. Chem Rev 2016;116(9):5464–519.
[25] Chen D, Feng H, Li J. Graphene oxide: preparation, functionalization, and electrochemical applications. Chem Rev 2012;112(11):6027–53.
[26] Wang Y, Lai Y, Wang S, Jiang W. Controlled synthesis and electromagnetic wave absorption properties of core-shell Fe_3O_4@SiO_2 nanospheres decorated graphene. Ceram Int 2017;43(2):1887–94.
[27] Wang Y, Peng Z, Jiang W. Size-controllable synthesis of Fe_3O_4 nanospheres decorated graphene for electromagnetic wave absorber. J Mater Sci Mater Electron 2016;27(6):6010–9.
[28] Kong L, Yin X, Yuan X, Zhang Y, Liu X, Cheng L, et al. Electromagnetic wave absorption properties of graphene modified with carbon nanotube/poly(dimethyl siloxane) composites. Carbon 2014;73:185–93.
[29] Liu J, Che R, Chen H, Zhang F, Xia F, Wu Q, et al. Microwave absorption enhancement of multifunctional composite microspheres with spinel Fe_3O_4 cores and anatase TiO_2 shells. Small 2012;8(8):1214–21.
[30] Mohammadi A, Barikani M, Lakouraj MM. Biocompatible polyurethane/thiacalix[4]arenes functionalized Fe_3O_4 magnetic nanocomposites: synthesis and properties. Mater Sci Eng C 2016;66:106–18.
[31] Thu TV, Sandhu A. Chemical synthesis of Fe_3O_4–graphene oxide nanohybrids as building blocks for magnetic and conductive membranes. Mater Sci Eng, B 2014;189:13–20.
[32] Su J, Cao M, Ren L, Hu C. Fe_3O_4–Graphene nanocomposites with improved lithium storage and magnetism properties. J Phys Chem C 2011;115(30):14469–77.
[33] Shi L, Zhao Y, Li Y, Han X, Zhang T. Octahedron Fe_3O_4 particles supported on 3D MWCNT/graphene foam: in-situ method and application as a comprehensive microwave absorption material. Appl Surf Sci 2017;416:329–37.
[34] Yadav RS, Kuřitka I, Vilcakova J, Skoda D, Urbánek P, Machovsky M, et al. Lightweight $NiFe_2O_4$-reduced graphene oxide-elastomer nanocomposite flexible sheet for electromagnetic interference shielding application. Compos B Eng 2019;166:95–111.
[35] Zhu L, Zeng X, Chen M, Yu R. Controllable permittivity in 3D Fe_3O_4/CNTs network for remarkable microwave absorption performances. RSC Adv 2017;7(43):26801–8.
[36] Agrawal PR, Kumar R, Teotia S, Kumari S, Mondal DP, Dhakate SR. Lightweight, high electrical and thermal conducting carbon-rGO composites foam for superior electromagnetic interference shielding. Compos B Eng 2019;160:131–9.
[37] Hu C, Mou Z, Lu G, Chen N, Dong Z, Hu M, et al. 3D graphene-Fe_3O_4 nanocomposites with high-performance microwave absorption. Phys Chem Chem Phys 2013;15(31):13038–43.
[38] Chen Y-H, Huang Z-H, Lu M-M, Cao W-Q, Yuan J, Zhang D-Q, et al. 3D Fe_3O_4 nanocrystals decorating carbon nanotubes to tune electromagnetic properties and enhance microwave absorption capacity. J Mater Chem 2015;3(24):12621–5.
[39] Ren F, Li Z, Xu L, Sun Z, Ren P, Yan D, et al. Large-scale preparation of segregated PLA/carbon nanotube composite with high efficient electromagnetic interference shielding and favourable mechanical properties. Compos B Eng 2018;155:405–13.
[40] Singh AP, Mishra M, Hashim DP, Narayanan TN, Hahm MG, Kumar P, et al. Probing the engineered sandwich network of vertically aligned carbon nanotube–reduced graphene oxide composites for high performance electromagnetic interference shielding applications. Carbon 2015;85:79–88.
[41] Singh AP, Garg P, Alam F, Singh K, Mathur RB, Tandon RP, et al. Phenolic resin-based composite sheets filled with mixtures of reduced graphene oxide, γ-Fe_2O_3 and carbon fibers for excellent electromagnetic interference shielding in the X-band. Carbon 2012;50(10):3868–75.
[42] Zhang H, Hong M, Chen P, Xie A, Shen Y. 3D and ternary rGO/MCNTs/Fe_3O_4 composite hydrogels: synthesis, characterization and their electromagnetic wave absorption properties. J Alloy Comp 2016;665:381–7.
[43] Zhao ZJ, Zhang BY, Du Y, Hei YW, Yi XS, Shi FH, et al. MWCNT modified structure-conductive composite and its electromagnetic shielding behavior. Compos B Eng 2017;130:21–7.
[44] Yang Y, Gupta MC, Dudley KL, Lawrence RW. Novel carbon nanotube – polystyrene foam composites for electromagnetic interference shielding. Nano Lett 2005;5(11):2131–4.
[45] Zhang H-B, Yan Q, Zheng W-G, He Z, Yu Z-Z. Tough graphene – polymer microcellular foams for electromagnetic interference shielding. ACS Appl Mater Interfaces 2011;3(3):918–24.
[46] Li N, Huang Y, Du F, He X, Lin X, Gao H, et al. Electromagnetic interference (EMI) shielding of single-walled carbon nanotube epoxy composites. Nano Lett 2006;6(6):1141–5.
[47] Staudenmaier L. Verfahren zur Darstellung der Graphitsäure. Ber Dtsch Chem Ges 1898;31(2):1481–7.
[48] Kumar R, Singh RK, Dubey PK, Singh DP, Yadav RM. Self-assembled hierarchical formation of conjugated 3D cobalt oxide nanobead–CNT–graphene nanostructure using microwaves for high-performance supercapacitor electrode. ACS Appl Mater Interfaces 2015;7(27):15042–51.
[49] Awasthi K, Kumar R, Tiwari RS, Srivastava ON. Large scale synthesis of bundles of aligned carbon nanotubes using a natural precursor: turpentine oil. J Exp Nanosci 2010;5(6):498–508.
[50] Kumar R, Singh RK, Tiwari RS. Growth analysis and high-yield synthesis of aligned-stacked branched nitrogen-doped carbon nanotubes using sesame oil as a natural botanical hydrocarbon precursor. Mater Des 2016;94:166–75.
[51] Kumar R, Dubey PK, Singh RK, Vaz AR, Moshkalev SA. Catalyst-free synthesis of a three-dimensional nanoworm-like gallium oxide–graphene nanosheet hybrid structure with enhanced optical properties. RSC Adv 2016;6(21):17669–77.
[52] Kumar R, da Silva ETSG, Singh RK, Savu R, Alaferdov AV, Fonseca LC, et al. Microwave-assisted synthesis of palladium nanoparticles intercalated nitrogen doped reduced graphene oxide and their electrocatalytic activity for direct-ethanol fuel cells. J Colloid Interface Sci 2018;515:160–71.
[53] Casiraghi C. Doping dependence of the Raman peaks intensity of graphene close to the Dirac point. Phys Rev B 2009;80(23):233407.
[54] Gopalsamy K, Balamurugan J, Thanh TD, Kim NH, Lee JH. Fabrication of nitrogen and sulfur co-doped graphene nanoribbons with porous architecture for high-performance supercapacitors. Chem Eng J 2017;312:180–90.
[55] Wang S, Zhang L, Xia Z, Roy A, Chang DW, Baek J-B, et al. BCN graphene as efficient metal-free electrocatalyst for the oxygen reduction reaction. Angew Chem Int Ed 2012;51(17):4209–12.
[56] Zhang G, Li J, Sha J, He C, Liu E, Zhao N, et al. Preparation of Fe_3O_4/rebar graphene composite via solvothermal route as binder free anode for lithium ion batteries. J Alloy Comp 2016;661:448–54.
[57] Li J, Zhang S, Chen C, Zhao G, Yang X, Li J, et al. Removal of Cu(II) and fulvic acid by graphene oxide nanosheets decorated with Fe_3O_4 nanoparticles. ACS Appl Mater Interfaces 2012;4(9):4991–5000.
[58] Zhu S, Guo J, Dong J, Cui Z, Lu T, Zhu C, et al. Sonochemical fabrication of Fe_3O_4 nanoparticles on reduced graphene oxide for biosensors. Ultrason Sonochem 2013;20(3):872–80.
[59] Zhao L, Gao M, Yue W, Jiang Y, Wang Y, Ren Y, et al. Sandwich-structured graphene-Fe_3O_4@carbon nanocomposites for high-performance lithium-ion batteries. ACS Appl Mater Interfaces 2015;7(18):9709–15.
[60] Wu Q-H, Qu B, Tang J, Wang C, Wang D, Li Y, et al. An alumina-coated Fe_3O_4-reduced graphene oxide composite electrode as a stable Anode for lithium-ion battery. Electrochim Acta 2015;156:147–53.
[61] Monazam ER, Breault RW, Siriwardane R. Kinetics of magnetite (Fe_3O_4) oxidation to hematite (Fe_2O_3) in air for chemical looping combustion. Ind Eng Chem Res 2014;53(34):13320–8.
[62] Kumar R, Singh RK, Vaz AR, Savu R, Moshkalev SA. Self-assembled and one-step synthesis of interconnected 3D network of Fe_3O_4/reduced graphene oxide nanosheets hybrid for high-performance supercapacitor electrode. ACS Appl Mater Interfaces 2017;9(10):8880–90.
[63] Wang L, Huang Y, Li C, Chen J, Sun X. Enhanced microwave absorption properties of N-doped graphene@PANI nanorod arrays hierarchical structures modified by Fe_3O_4 nanoclusters. Synth Met 2014;198:300–7.
[64] Qu B, Zhu C, Li C, Zhang X, Chen Y. Coupling hollow Fe_3O_4–Fe nanoparticles with graphene sheets for high-performance electromagnetic wave absorbing material. ACS Appl Mater Interfaces 2016;8(6):3730–5.
[65] Wang T, Zhang L, Wang H, Yang W, Fu Y, Zhou W, et al. Controllable synthesis of hierarchical porous Fe_3O_4 particles mediated by poly(diallyldimethylammonium chloride) and their application in arsenic removal. ACS Appl Mater Interfaces 2013;5(23):12449–59.
[66] Zong M, Huang Y, Zhao Y, Sun X, Qu C, Luo D, et al. Facile preparation, high microwave absorption and microwave absorbing mechanism of RGO-Fe_3O_4 composites. RSC Adv 2013;3(45):23638–48.
[67] Chen M, Hou C, Huo D, Fa H, Zhao Y, Shen C. A sensitive electrochemical DNA biosensor based on three-dimensional nitrogen-doped graphene and Fe_3O_4 nanoparticles. Sensor Actuator B Chem 2017;239:421–9.
[68] He F, Lam K, Ma D, Fan J, Chan LH, Zhang L. Fabrication of graphene nanosheet (GNS)–Fe_3O_4 hybrids and GNS–Fe_3O_4/syndiotactic polystyrene composites with high dielectric permittivity. Carbon 2013;58:175–84.
[69] Fujii T, de Groot FMF, Sawatzky GA, Voogt FC, Hibma T, Okada K. *In situ* XPS

analysis of various iron oxide films grown by NO_2-assisted molecular-beam epitaxy. Phys Rev B 1999;59(4):3195–202.
[70] Luo J, Liu J, Zeng Z, Ng CF, Ma L, Zhang H, et al. Three-dimensional graphene foam supported Fe_3O_4 lithium battery anodes with long cycle life and high rate capability. Nano Lett 2013;13(12):6136–43.
[71] Rooj A, Roy M, Bhattacharjee A. Thermal decomposition reaction of ferrocene in the presence of oxalic acid. Int J Chem Kinet 2017;49(5):319–32.
[72] Barreiro A, Hampel S, Rümmeli MH, Kramberger C, Grüneis A, Biedermann K, et al. Thermal decomposition of ferrocene as a method for production of single-walled carbon nanotubes without additional carbon sources. J Phys Chem B 2006;110(42):20973–7.
[73] Verissimo C, Aguiar MR, Moshkalev SA. Formation of catalyst nanoparticles and nucleation of carbon nanotubes in chemical vapor deposition. J Nanosci Nanotechnol 2009;9(7):4459–66.
[74] Srivastava SK, Mittal V. Advanced nanostructured materials in electromagnetic interference shielding. Hybrid nanomaterials. John Wiley & Sons, Inc.; 2017. p. 241–320.
[75] Lee SH, Yu S, Shahzad F, Kim WN, Park C, Hong SM, et al. Density-tunable lightweight polymer composites with dual-functional ability of efficient EMI shielding and heat dissipation. Nanoscale 2017;9(36):13432–40.
[76] Singh AP, Gupta BK, Mishra M, Govind, Chandra A, Mathur RB, et al. Multiwalled carbon nanotube/cement composites with exceptional electromagnetic interference shielding properties. Carbon 2013;56:86–96.
[77] Shahzad F, Alhabeb M, Hatter CB, Anasori B, Man Hong S, Koo CM, et al. Electromagnetic interference shielding with 2D transition metal carbides (MXenes). Science 2016;353(6304):1137–40.
[78] Biswas S, Arief I, Panja SS, Bose S. Electromagnetic screening in soft conducting composite-containing ferrites: the key role of size and shape anisotropy. Materials Chemistry Frontiers 2017;1(12):2574–89.
[79] Basuli U, Chattopadhyay S, Nah C, Chaki TK. Electrical properties and electromagnetic interference shielding effectiveness of multiwalled carbon nanotubes-reinforced EMA nanocomposites. Polym Compos 2012;33(6):897–903.
[80] Kumaran R, kumar SD, Balasubramanian N, Alagar M, Subramanian V, Dinakaran K. Enhanced electromagnetic interference shielding in a Au–MWCNT composite nanostructure dispersed PVDF thin films. J Phys Chem C 2016;120(25):13771–8.
[81] Zhang H, Zhang G, Li J, Fan X, Jing Z, Li J, et al. Lightweight, multifunctional microcellular PMMA/Fe_3O_4@MWCNTs nanocomposite foams with efficient electromagnetic interference shielding. Compos Appl Sci Manuf 2017;100:128–38.
[82] Liang J, Wang Y, Huang Y, Ma Y, Liu Z, Cai J, et al. Electromagnetic interference shielding of graphene/epoxy composites. Carbon 2009;47(3):922–5.
[83] Gedler G, Antunes M, Velasco JI, Ozisik R. Enhanced electromagnetic interference shielding effectiveness of polycarbonate/graphene nanocomposites foamed via 1-step supercritical carbon dioxide process. Mater Des 2016;90:906–14.
[84] Li X-H, Li X, Liao K-N, Min P, Liu T, Dasari A, et al. Thermally annealed anisotropic graphene aerogels and their electrically conductive epoxy composites with excellent electromagnetic interference shielding efficiencies. ACS Appl Mater Interfaces 2016;8(48):33230–9.
[85] Shen B, Zhai W, Tao M, Ling J, Zheng W. Lightweight, multifunctional polyetherimide/graphene@Fe_3O_4 composite foams for shielding of electromagnetic pollution. ACS Appl Mater Interfaces 2013;5(21):11383–91.
[86] Xu H-L, Bi H, Yang R-B. Enhanced microwave absorption property of bowl-like Fe_3O_4 hollow spheres/reduced graphene oxide composites. J Appl Phys 2012;111(7):07A522.
[87] Chen H, Huang Z, Huang Y, Zhang Y, Ge Z, Qin B, et al. Synergistically assembled MWCNT/graphene foam with highly efficient microwave absorption in both C and X bands. Carbon 2017;124:506–14.
[88] Zhan Y, Zhao R, Lei Y, Meng F, Zhong J, Liu X. Preparation, characterization and electromagnetic properties of carbon nanotubes/Fe_3O_4 inorganic hybrid material. Appl Surf Sci 2011;257(9):4524–8.
[89] Sun X, He J, Li G, Tang J, Wang T, Guo Y, et al. Laminated magnetic graphene with enhanced electromagnetic wave absorption properties. J Mater Chem C 2013;1(4):765–77.
[90] Li Q, Chen L, Ding J, Zhang J, Li X, Zheng K, et al. Open-cell phenolic carbon foam and electromagnetic interference shielding properties. Carbon 2016;104:90–105.
[91] Pawar SP, Marathe DA, Pattabhi K, Bose S. Electromagnetic interference shielding through MWNT grafted Fe_3O_4 nanoparticles in PC/SAN blends. J Mater Chem 2015;3(2):656–69.
[92] Mishra M, Singh AP, Singh BP, Singh VN, Dhawan SK. Conducting ferrofluid: a high-performance microwave shielding material. J Mater Chem 2014;2(32):13159–68.
[93] Wen B, Wang XX, Cao WQ, Shi HL, Lu MM, Wang G, et al. Reduced graphene oxides: the thinnest and most lightweight materials with highly efficient microwave attenuation performances of the carbon world. Nanoscale 2014;6(11):5754–61.
[94] Pawar SP, Biswas S, Kar GP, Bose S. High frequency millimetre wave absorbers derived from polymeric nanocomposites. Polymer 2016;84:398–419.